J Mater Sci: Mater Electron (2021) 32:9126–9148

Crystal growth and properties measurements of nickel doped potassium dihydrogen citrate crystals

N. D. Pandya[1], J. H. Joshi[2,*], H. O. Jethva[1,*], and M. J. Joshi[1]

[1] Department of Physics, Saurashtra University, Rajkot 360 005, India
[2] Physics & Ballistic Division, Forensic Science Laboratory, Ahmadabad 380 016, India

Received: 6 January 2021
Accepted: 18 February 2021
Published online: 5 March 2021

ABSTRACT

Potassium dihydrogen citrate (KDC) is well-recognized food additive and mineral found in various fruits which make it interesting to study its properties under the influence of toxic metal doping. Pure and different mol% Ni^{2+}-doped KDC crystals were grown using slow-solvent evaporation technique at room temperature. The grown crystals exhibits needle-shaped morphology. EDAX analysis reveals apparent concentration of Ni^{2+} in different mol% Ni^{2+}-doped KDC. Indexing of powder XRD patterns of pure and different mol% Ni^{2+}-doped KDC reveals triclinic symmetry of grown crystals. W–H analysis reveals presence of lattice strain under the incorporation of Ni^{2+} doping in the host lattice of KDC. Bond assignments corresponding to various functional groups present in grown crystals is studied using the FT-IR spectroscopic study. The modification in thermal stability of KDC due to Ni^{2+} doping is studied using TGA analysis. The SEM study has shown grain growth in KDC crystal due to Ni^{2+} doping. The presence of grain, grain boundary effect and relaxation mechanism involved in transport properties of pure and different mol% Ni^{2+} doped KDC is reported using the Impedance–Modulus spectroscopic studies. Dielectric studies reveal modification in dielectric constant, dielectric loss and a.c. conductivity of KDC due to Ni^{2+} doping. The structural defect mechanism is well studied using the photoluminescence.

1 Introduction

Potassium dihydrogen citrate (KDC) is widely studied due to its key role of food additive in varieties of food products as well as its natural existence in various fruits [1, 2]. KDC also find its importance due its medical and pharmaceutical applications for the treatment of kidney stone, gaut and acidosis caused by kidney disease [3].

While looking for toxicity point of view, Nickel compounds are characterized due to their environmental fate. Nickel compounds exists in the earth's crust and 8.5 million Nickel get mixed with atmosphere via natural discharges such as windblown dust and volcanic eruptions and vegetation each year

Address correspondence to E-mail: jaydeep_joshi1989@yahoo.com; hojethva@rediffmail.com

https://doi.org/10.1007/s10854-021-05580-8

[4]. Thus nickel can be considered as a ubiquitous trace element and most common source of metal allergy. Mankind can be exposed to nickel allergy because of presence of nickel in most of the dietary items [5]. As the KDC is important food material, it is essential to study its participation in compound formation with nickel due to food pollutant behavior of nickel.

The Ni^{2+} doping in pure KDC is aimed to study role of Ni^{2+} to modify certain structural, spectroscopic, thermal, electrical and luminescence properties by inducing defect and introducing the toxic element in the host compound.

It is revealed from the literature survey that very few reports are available on pure and metal-doped KDC. These reports comprises of the studies of crystal structure of citrate and double citrate salt [6, 7] and solubility [8]. Furthermore, while referring the recent reports, structural, micro structural and thermal studies are explained by various authors [9]. In addition to that, study is also carried out on optical and magnetic properties of VO^{2+} doped and Cu^{2+} doped KDC crystals [10–12].

It should be noted that, none of the above-mentioned authors have investigated role of toxic bivalent metal ions in inducing structural defect and it's chemistry in KDC crystal. Furthermore, under the effect of bivalent Ni^{2+} doping, authors are tempted to study effect of grain and grain boundary mechanism on certain physio-chemical properties such as structural, spectroscopic, thermal, luminescent and dielectric by considering defect-oriented approach.

2 Experimental technique

For the growth of pure KDC crystal and different mol%, i.e. 0.4 mol%, 0.6 mol% and 0.8 mol% nickel doped KDC crystals; the slow solvent evaporation technique was used. Initially, to prepare the saturated solution of the source material, i.e. pure KDC at room temperature, it was dissolved gravimetrically into 400 ml distilled water. The molar concentration of KDC is kept constant in aqueous solution which is 2 mol. The solution was continuously stirred using magnetic stirrer for 4 h to achieve homogeneous solution. The saturated solution was filtered twice with a Whatman (cat No. 1001 125) filter paper of 12.5 cm diameter. Then, the solution was subdivided into four beakers; each was containing 100 ml pure KDC solution. Out of these four beakers, one was used for the growth of pure KDC crystal. This beaker was shielded with porous lid having 4 to 5 pinholes and it was kept into dust and disturbance free place for the evaporation. In the remaining other three beakers containing pure KDC solution, 0.1048 g, 0.1572 g and 0.2096 g nickel sulphate was added. Nickel sulphate added beakers were again stirred for nearly 4 h and then filtered. These beakers were shielded with porous lid having 4 to 5 pinholes and kept into dust and disturbance free place for the evaporation. After 30 days, good quality and transparent crystals of pure and nickel doped KDC were harvested from the solutions.

Figure 1a shows the grown crystal of pure KDC, while Fig. 1b, c and d show 0.4 mol%, 0.6 mol% and 0.8 mol% nickel doped KDC crystal, respectively.

The grown crystals of pure and different mol% Ni^{2+} doped KDC possesses needle-shaped morphology and transparent in nature.

The grown crystals were characterized by EDAX, Powder XRD, FTIR, thermal analysis, impedance and modulus analysis, dielectric analysis and PL study. The EDAX was carried out by using FEG Nano Nova SEM 450 instrument with 2 nm resolution at 30 kV. The Powder XRD patterns were recorded on PANalytical X'pert pro set up using Cu Kα radiation within 2θ range 10° to 50° in steps of 0.02° s^{-1}. The data of $\%T$ were recorded on Thermo Nicolet Avtar 370 set up within the frequency range 4000 cm^{-1} to 400 cm^{-1} in KBr medium. The TGA was conducted on Perkin Elmer STA-8000 set up from room temperature to 700 °C at heating rate 15 °C/min in the nitrogen atmosphere. The dielectric study was carried out using the Precision LCR meter Agilent 4284A instrument and a conventional sample holder within the frequency range 100 Hz to 1 MHz at room temperature. A die having diameter of 13 mm was used to pelletize each sample by applying 2 tone of pressure for 5 min. Before placing the samples turn by turn between sample holder, silver paste was applied on each pellet to ensure proper electrical connection. The photoluminescence emission and absorption spectra were recorded at room temperature using Shimadzu RF-5301 PC spectro-fluro-photometer and Xe is used as the excitation source.

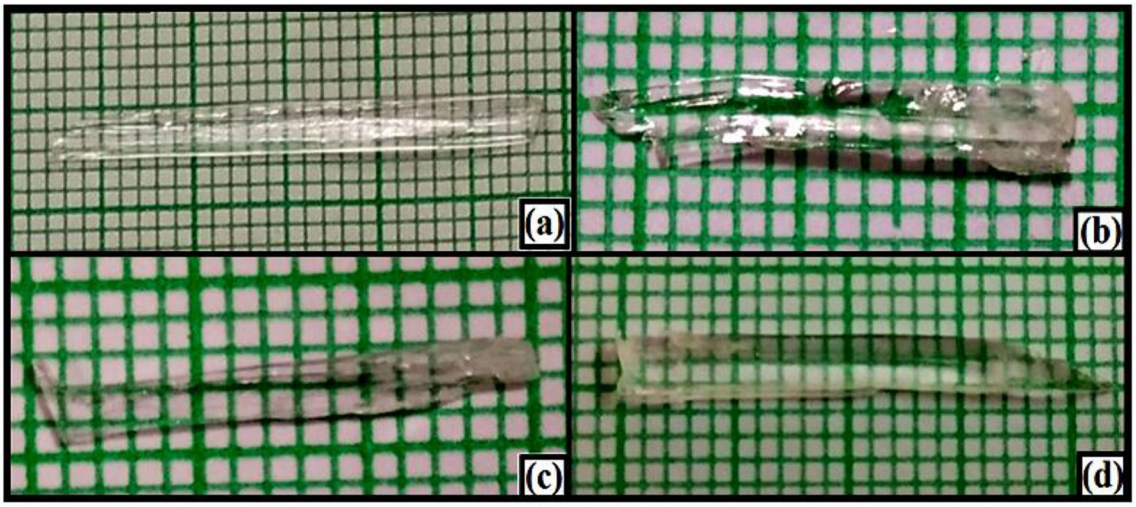

Fig. 1 Grown crystals of **a** pure KDC, **b** 0.4 mol% nickel doped KDC, **c** 0.6 mol% nickel doped KDC and **d** 0.8 mol% nickel doped KDC

3 Result and discussion

3.1 EDAX analysis

The EDAX spectrum of pure and different mol% Ni^{2+} doped KDC is shown in Fig. 2.

In order to find out the elemental composition of the grown crystals, the EDAX study was carried out. In the Table 1, observed atomic wt% of potassium and nickel from EDAX and estimated stoichiometric formula for all the crystals.

From the EDAX result shown in the Table 1, the presence of nickel confirms the successful doping of nickel in the crystalline lattice of pure KDC. Further, as the mol% of nickel is increased from 0.4 to

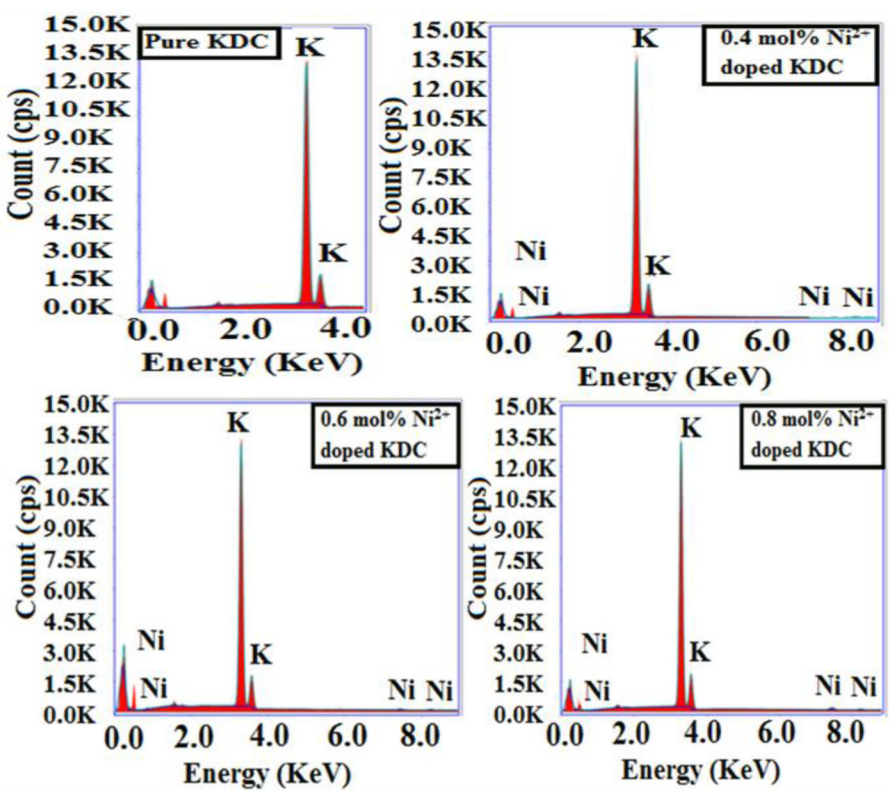

Fig. 2 EDAX spectrum of pure and (0.4, 0.6, 0.8) mol% Ni^{2+} doped KDC

Table 1 EDAX result and estimated stoichiometric formula

Sample Nos	Sample name	Observed atomic weight (%) (from EDAX)		Estimated stoichiometric formula
		Element		
		K	Ni	
1	Pure KDC	100	0	$C_6H_7KO_7{\cdot}nH_2O$
2	0.4 mol% Ni doped KDC	98.81	1.19	$C_6H_5K_{(0.9881)}Ni_{(0.0119)}\ O_7{\cdot}nH_2O$
3	0.6 mol% Ni doped KDC	98.27	1.73	$C_6H_5K_{(0.9827)}Ni_{(0.0173)}\ O_7{\cdot}nH_2O$
4	0.8 mol% Ni doped KDC	97.21	2.79	$C_6H_5K_{(0.9721)}Ni_{(0.0279)}\ O_7{\cdot}nH_2O$

0.8 mol%, the corresponding increase in the atomic wt% of nickel is also observed from the EDAX result. The atomic wt% of potassium in the crystalline lattice is very high compared to nickel in the nickel-doped KDC crystals. The concentration of solution of KDC is 2 mol. To grow 0.4 mol%, 0.6 mol% and 0.8 mol% nickel doped KDC crystals, the amount of salt of nickel dissolved is less than 1 g, resulting into the presence of nickel in very less amount and the same is confirmed by EDS analysis.

3.2 Powder XRD study

Figure 3 shows the Powder XRD patterns of pure KDC and different mol% nickel-doped KDC, while the unit cell parameters are represented in Table 2.

From the XRD pattern shown in the Fig. 3, it can be seen that no additional phase is found to be present in the different mol% nickel doped KDC crystals, indicating all the crystals possess a single phase nature. When nickel in different mol% is doped into pure KDC, the intensity as well as position of major peaks of pure KDC is observed to change. For example, in pure KDC, peaks (2−11) at 18.201°, (0−31) at 20.69°, (1−42) at 30.05° are observed to shift little towards higher angle side with reduction in intensity in nickel doped KDC. The peak (−210) at 19.1° in pure KDC is observed to shift little towards higher angle side with increase in intensity in nickel doped KDC. The peak (032) at 27.48° in pure KDC is observed to shift little towards higher angle side with

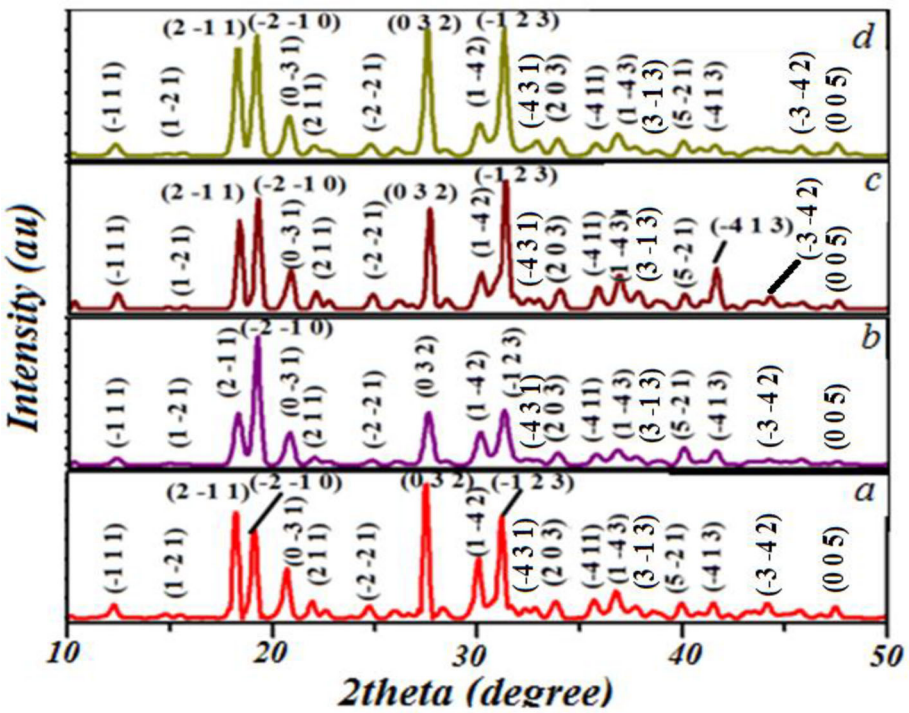

Fig. 3 Powder XRD patterns (a) sample 1. Pure KDC (b) sample 2. 0.4 mol% Ni doped KDC (c) sample 3. 0.6 mol% Ni doped KDC (d) sample 4. 0.8 mol% Ni doped KDC

Table 2 Unit cell parameters of pure and nickel doped KDC crystals

Sample name	a (Å)	b (Å)	c (Å)	α	β	γ	Unit cell volume (Å^3)
Pure KDC	11.820	14.970	9.442	91.6	93.35	110	1565.25
0.4 mol% Ni doped KDC	11.803	14.967	9.436	91.20	93.45	109.90	1563.04
0.6 mol% Ni doped KDC	11.817	14.963	9.436	91.20	93.45	109.90	1564.48
0.8 mol% Ni doped KDC	11.819	14.961	9.437	91.13	93.45	109.90	1564.79

reduction in peak intensity in nickel doped KDC, except (0.8 mol% Ni doped KDC) in which increased intensity is observed. The peak (−123) at 31.19° in pure KDC is observed to shift little towards higher angle side with increase in intensity in different mol% nickel doped KDC except the (0.4 mol% Ni-doped KDC) in which decreased intensity is observed. Now, the scattering intensities for X-rays are directly related to the number of electrons in the atom. Hence, light atoms scatter X-rays weakly, while heavy atoms scatter X-rays more effectively. Therefore, the increase in intensity of peak (−210) of pure KDC in nickel doped KDC may be due to the presence of nickel at that particular plane, while the reduction in the intensity of peaks (2−11), (0−31) and (1−42) of pure KDC in nickel doped KDC may be due to the presence of potassium in higher concentration at that particular plane. The reduction in the intensity of peak (032) of pure KDC for 0.4 mol% and 0.6 mol% nickel-doped KDC indicates the effect of potassium and increase in intensity of the same peak for 0.8 mol% nickel doped KDC indicates the effect of nickel. Similarly, increase in intensity of peak (123) of pure KDC for 0.6 mol% and 0.8 mol% nickel doped KDC indicates the effect of nickel and reduction in intensity of the same peak in 0.4 mol% nickel-doped KDC indicates the effect of potassium.

The above-mentioned changes in the peak intensity reflect that the total scattering from each crystal planes is different, which depends on the distribution of the atoms potassium and nickel in the crystal structure. Further, peak shifting towards higher 2θ value indicating suppression in cell volume of nickel doped KDC crystals as mentioned in Table 2 due to doping of smaller nickel ion (72 pm) compared to larger potassium ion (138 pm), resulting into decrease in lattice parameters of nickel doped KDC as mentioned in Table 2 and it indicates the incorporation of nickel into lattice of potassium dihydrogen citrate. Though, the peak shifting is observed on doping of nickel in pure KDC, the crystal structure remains unchanged.

To estimate the lattice strain of the pure and different mol% nickel-doped KDC crystals, the Williamson–Hall method is applied [13]. The strain was calculated from the slope of the Williamson–Hall plot, The value of strain is mentioned in the Table 3.

It can be seen from the Table 3 that the lowest value of strain is obtained for the pure KDC, indicating minimum grain distortion, point defect density and residual stresses in the lattice.

3.3 SEM study

Figure 4 shows SEM images of pure and different mol% Ni^{2+} doped KDC crystals. Figure 4a reveals agglomeration of crystallites in pure KDC. However, Fig. 4b–d shows that crystallites remain distinguishable in (0.4 to 0.8) mol% Ni^{2+}-doped KDC crystals along with slip bands in their background [10].

SEM images clearly indicates increase in crystallize in different mol% Ni^{2+} doped KDC crystals with compared to pure KDC crystal. To confirm increase in crystallite size (D) due to Ni^{2+} doping in KDC, Debye–Scherrer's equation [14] is employed to estimate crystallite size (D) in grown crystals expressed as below:

$$D = \frac{K\lambda}{B\cos\theta}, \tag{1}$$

Table 3 Strain values for pure and Ni^{2+} doped KDC crystals

Sample	Lattice strain (η)
Pure KDC	0.00887
0.4 mol% Ni doped KDC	0.00942
0.6 mol% Ni doped KDC	0.01368
0.8 mol% Ni doped KDC	0.01789

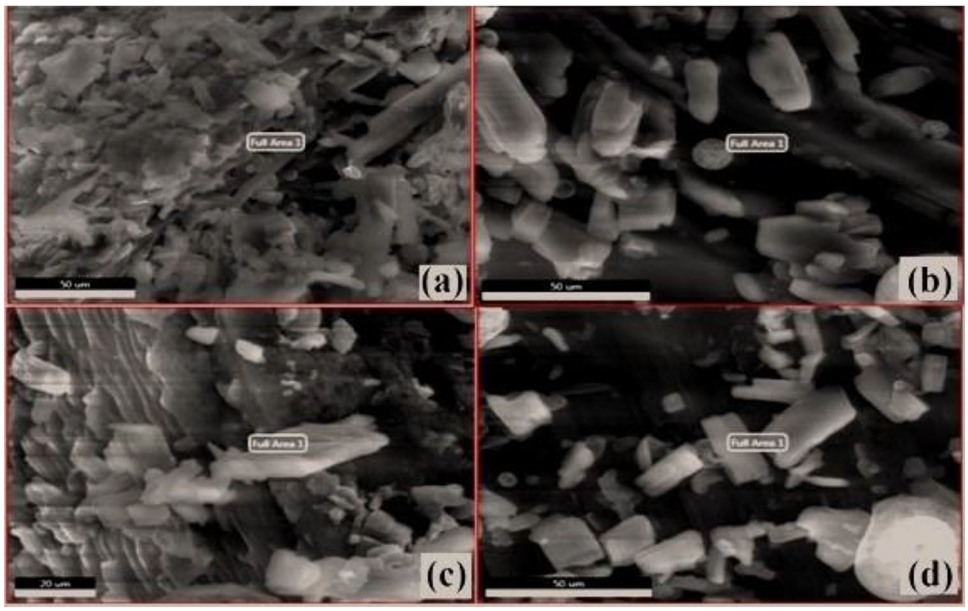

Fig. 4 SEM images of **a** pure, **b** 0.4, **c** 0.6 and **d** 0.8 mol% Ni^{2+} doped KDC crystals

where λ is the X-ray source wavelength, β is the full width half maximum (FWHM) for the high intensity diffraction peak, θ is the diffraction angle and K is Scherrer's constant which is usually considered as 0.9. The crystallite size estimated from Debye–Scherrer's equation is listed in Table 4.

Table 4 reveal that the crystallite size of pure and different mol% Ni^{2+}-doped KDC estimated by Scherrer's equation indicates increase in crystallite size which is also revealed by SEM images. Thus, estimated values of crystallite size from Scherrer's equation are in correlation with SEM images.

The powder XRD pattern revealed decrease in FWHM of maxima which can be correlated with increase in crystallite size shown by SEM images and estimated by Scherrer's equation.

3.4 FTIR spectroscopy study

Figure 5 shows the FTIR spectra of pure and different mol% nickel doped KDC. The observed absorption frequencies and their assignments in relation to their characteristic vibrational modes are listed in Table 5.

Table 4 Estimated values of crystallite size for pure and (0.4, 0.6, 0.8) mol% Ni^{2+} doped KDC crystals

Sample name	D (nm)
Pure KDC	0.511
0.4 Ni^{2+}: KDC	0.786
0.6 Ni^{2+}: KDC	1.015
0.8 Ni^{2+}: KDC	1.073

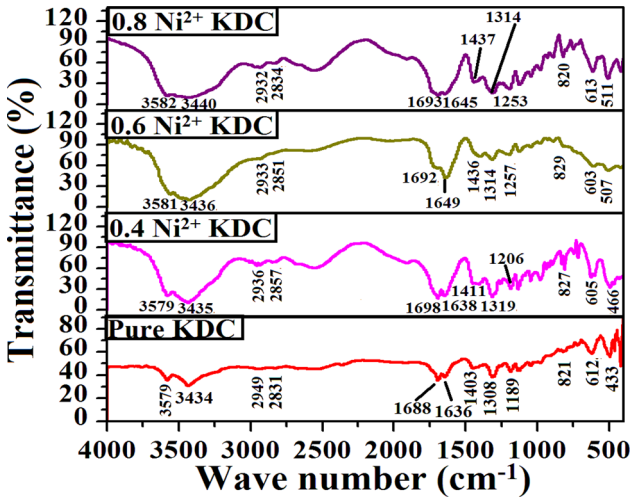

Fig. 5 FTIR spectra of pure and (0.4, 0.6, 0.8) mol% Ni^{2+} doped KDC

The broad absorption observed between 2500 and 3600 cm^{-1} corresponds to hydroxy group, H-bonded O–H stretching vibrations [15] due to water of crystallization associated with the crystals, which confirms the hydrous nature of all the compounds. The bands observed between 2830 and 2980 cm^{-1} can be attributed to the asymmetrical and symmetrical C–H stretching vibrations of citric acid, while the bending and deformation vibrations of the same are observed within 600 to 890 cm^{-1} wave number [15].

The C=O group stretching vibrations are observed between 1635 and 1725 cm^{-1} [15]. C–OH bending vibrations of COOH are observed within the

Table 5 Assignments of functional groups with frequency

Assignments	Wave numbers (cm^{-1})			
	Pure KDC	0.4 Ni^{2+} KDC	0.6 Ni^{2+} KDC	0.8 Ni^{2+} KDC
O–H Stretching	3579, 3434, 2515	3579, 3435, 2547	3581, 3436, 2559	3582, 3440, 2571
Asymmetrical C–H stretching	2949	2977, 2936	2961, 2933	2968, 2932
Symmetrical C–H stretching	2831	2857	2851	2834
C=O stretching	1688, 1636	1722, 1698	1692, 1649	1693, 1645
C–OH bending vibrations	1403	1411	1436	1437
C–C stretching	1308, 1189, 1123, 1045	1344, 1319, 1206, 1111, 1045	1314, 1257, 1184, 1132, 1085, 1047	1314, 1253, 1193, 1122, 1044
O–H bending in-plane	1308, 1255	1344, 1319	1314, 1257	1314, 1253
C–O stretching	1045, 1123	1045, 1111, 1206	1047, 1085, 1132	978, 1044, 1122,
C–H bending vibrations	723, 755, 821, 840, 880	718, 748, 787, 827, 894	716, 743, 810, 829, 894	748, 799, 820, 889
C–H deformation	680, 617	679, 655, 605	603, 626	613
O–H bending out-of-plane	717, 612,	718, 679, 655, 605	716, 626, 603,	713, 613
K–O and Ni–O stretching	433, 407	492, 466	560, 507	568, 511

frequency range 1400 to 1440 cm^{-1}, while O–H in-plane and out-of-plane bending vibrations of the same are observed within the frequency range 1250 to 1350 cm^{-1} and 600 to 720 cm^{-1}, respectively [15].

The citrate crystals also possess the C–C group and therefore, one can assign the C–C stretching vibrations also. But, the bands assigned to C–C stretching vibrations are weak and appear in the broad region of 1200 to 800 cm^{-1}; with overlapping to some other absorption bands, generally they are little value for identification [16].

The citrate crystals also possess the C–C group and therefore, one can assign the C–C stretching vibrations also. But, the bands assigned to C–C stretching vibrations are weak and appear in the broad region of 1200 to 800 cm^{-1}; with overlapping to some other absorption bands, generally they are little value for identification [16]. Absorption wave numbers nearly and below 600 cm^{-1} are assigned to metal–oxygen vibrations as the same can be assigned in the case of pure and mixed metal-tartrate crystals [17–19]. Comparing the different absorptions of different mol% Ni-doped KDC crystals in FTIR spectra with pure KDC crystals, one can conclude that there is no major effect of nickel doping on the different absorptions in FTIR spectra. As per one study, the low concentration of impurity or dopant does not affect much the FTIR spectra [20]. However, minor shift in majority of absorption bands towards higher wave number are observed, while metal–oxygen vibrations shift appreciably towards higher wave number. The shifting of the characteristic bands indicates the perturbation caused by the doping of nickel in the lattice of pure KDC, which depends on the electro negativity of neighboring groups of atoms, the spatial geometry of the molecule or mechanical mixing of vibrational modes [21, 22]. The atomic mass number of potassium and nickel are 39.0983 u and 58.6934 u, respectively. Hence, doping of more massive nickel in pure KDC expected to cause alternations in the molecular geometry, bond lengths and mechanical vibrations, resulting into slight alternations in the FTIR spectra of nickel doped KDC. On the basis of the above FTIR results, the expected molecular structure of nickel-doped KDC can be represented as shown in the Fig. 6.

From the expected molecular structure, it is evident that some of the carboxylate groups of the citrate anion are coordinating with nickel ions in the nickel-doped KDC, although the presence of carboxylate,

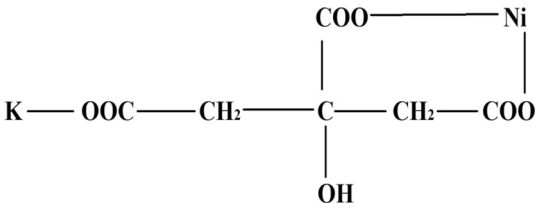

Fig. 6 Expected molecular structure of nickel doped KDC

not bound to the nickel ions cannot be excluded because of very high concentration carboxylate groups in the saturated solution of pure KDC compare to doped nickel ions in very low concentration.

The relationship between force constant and absorption frequency is expressed by the following relation:

$$v = 1303\sqrt{F\left(\frac{1}{M_1}+\frac{1}{M_2}\right)}, \quad (2)$$

where v is the absorption frequency in (cm^{-1}), $1303 = (N_A \times 10)^{1/2}/2\pi c$, M_1 and M_2 are the atomic masses of the atoms (u). From the above equation, the calculated values of force constant of Ni^{2+} doped KDC with compared to pure KDC are listed in Table 5 (Table 6).

From the above values of force constant of O–H bond, it can be concluded that hydrogen bond defect (D-defect) caused by Ni^{2+} doping increases the force constant of O–H bond.

3.5 Thermal analysis

Figure 7 shows the thermo-gram of pure and different mol% nickel-doped KDC crystals.

The thermo-gram of pure KDC indicates that the crystal of pure KDC is stable up to 60 °C and then starts losing water molecules within temperature range 67 to 88 °C. Within this temperature range, sample losses 3.5 water molecules, which results into nearly 15% weight loss of the sample. Then within

Table 6 O–H bond force constant of pure and Ni^{2+} doped KDC crystals

Sample name	Force constant (Nm^{-1})
Pure KDC	658.91
0.4 Ni^{2+}: KDC	659.35
0.6 Ni^{2+}: KDC	659.74
0.8 Ni^{2+}: KDC	661.28

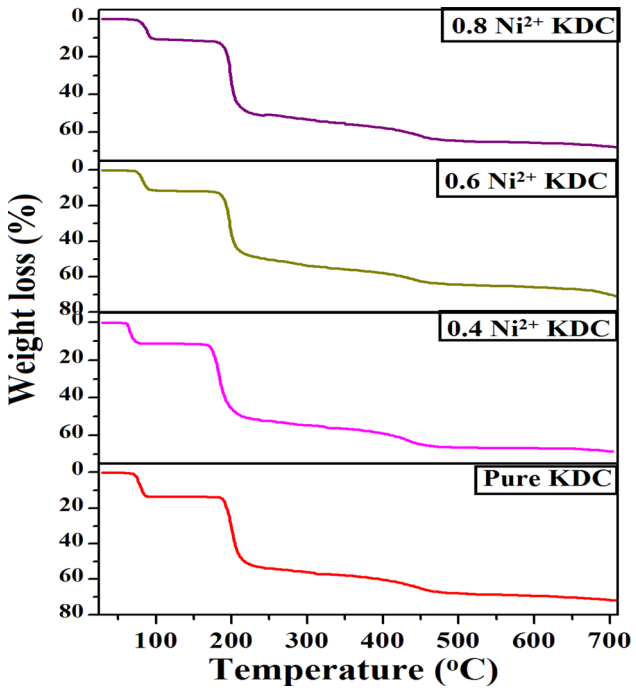

Fig. 7 TG curves of pure and (0.4, 0.6, 0.8) mol% Ni^{2+} doped KDC

temperature range 88 to 186 °C, sample remains stable, i.e. no decomposition of the sample takes place. During the second stage of decomposition between 186 and 300 °C, the sample becomes anhydrous and converts into carbonate form with the loss of 56% of its original weight. Within temperature range 300 to 500 °C, the sample shows slow decomposition process and convert into oxide form with the loss of nearly 70% of its original weight. Then, up to the upper limit of the temperature, i.e., 700 °C, the sample remains stable. From the analysis, it is found that nearly 4 water molecules are associated with the crystal.

Compared to pure KDC, (0.4, 0.6, 0.8) mol% nickel doped KDC remain stable up to temperature, 65 °C, 71 °C and 74 °C, respectively. This shows that the thermal stability of different mol% nickel-doped KDC crystal slightly increases. Then within temperature range, 65 to 84 °C, 71 to 87 °C and 74 to 93 °C, samples 2, 3 and 4 looses 2 water molecules, which results into nearly 11% weight loss of the samples. Then, within temperature range 84 to 183 °C, all the three samples remain stable. During the second stage of decomposition within temperature range 177 to 243 °C, all the three samples become anhydrous and convert into oxalate form showing weight loss of

nearly 50% of their original weight. During the third stage of decomposition up to temperature 400 °C, all the three samples convert into carbonate form showing the weight loss of 58% of their original weight. Final stage of decomposition of all the three samples into oxide of potassium–nickel observed within 400 to 500 °C and after that all the three samples remain stable up to the upper limit of temperature, i.e., 700 °C. From the analysis, nearly 5 water molecules are observed to be associated with the nickel-doped KDC crystals. Slight increase in thermal stability and existence of additional stage of oxalate confirms the effect of doping of nickel in the crystal lattice of pure KDC.

The percentages of the mass loss in the different stages of decomposition of pure and different mol% nickel doped KDC crystal are shown in the Table 7.

Effect of toxicity of Ni^{2+} is reflected in TGA studies as it finds possibilities to remain in food even after cooking; it slightly increases thermal stability of KDC.

3.6 Complex impedance and modulus analysis

The complex impedance spectroscopy distinguishes the grain, grain boundary and electrode properties of the material. By employing complex impedance study, various electrical phenomena and their correlation with crystal can be modeled by constructing equivalent electrical circuit [23].

The complex impedance is expressed by $Z^* = Z' - jZ''$; where Z' and Z'' are termed as real and imaginary parts of impedance, respectively [24].

Where Z' and Z'' are expressed by following equation

$$Z' = \frac{M''}{\omega C_0} \quad \text{and} \quad Z'' = -\frac{M'}{\omega C_0}, \tag{3}$$

where M' is real part of complex modulus, M'' is imaginary part of complex modulus, ω is angular frequency of applied field and C_0 is vacuum capacitance.

In the present study, the complex impedance and modulus study of pure KDC crystal of sample 1 and different mol% nickel-doped KDC crystals of samples 2 to 4 were carried out at room temperature within the frequency range 100 Hz to 1 MHz.

3.7 Frequency dependence of Z′

Figure 8 shows the dependence of real (Z') component of complex impedance at room temperature of pure and different mol% Ni-doped KDC.

Table 7 Observed and calculated mass loss (%) in the different stages of decomposition

Sample	Stage	Temperature range (°C)	Observed mass loss (%)	Calculated mass loss (%)	Loss of molecules
Pure KDC	I	67–88	13.5	14.6	$3H_2O$
	II	186–300	56.1	55.5	H_2O, CH_4, CO and H_2
	III	300–500	69.4	69.7	CO_2
0.4 mol% Ni doped KDC	I	65–84	11.3	11.2	$2H_2O$
	II	177–232	51	49.9	$3H_2O$, CH_4, CO and H_2
	III	232–400	58.76	58.2	CO
	IV	400–500	66.9	67.3	CO
0.6 mol% Ni doped KDC	I	71–87	11.7	11	$2H_2O$
	II	182–243	50	49.7	$3H_2O$, CH_4, CO and H_2
	III	243–400	58.2	58	CO
	IV	400–500	65	66	CO
0.8 mol% Ni doped KDC	I	74–93	10.8	11.4	$2H_2O$
	II	183–213	48	50	$3H_2O$, CH_4, CO and H_2
	III	213–400	57.7	56.7	CO
	IV	400–500	64.6	65.6	CO

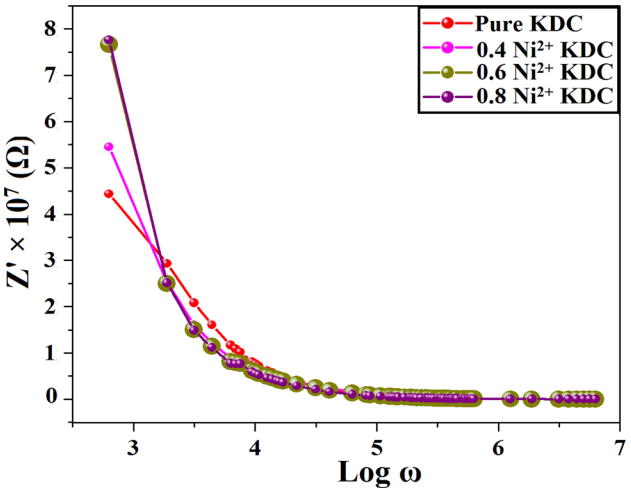

Fig. 8 Plot of Z' versus logω of pure and (0.4, 0.6, 0.8) mol% Ni^{2+} doped KDC

It is observed from the plot that dramatical decrease in the value of Z' is observed with increase in frequency for all the samples. This indicates an increase in the a.c. conductivity of all samples with increase in frequency [25] and the presence of space charge conduction at low frequencies. At higher frequencies, Z' achieves nearly a very low constant value and becomes almost independent of frequency for all the samples, which indicates the inability of space charges to follow the high-frequency fields [26, 27]. At lower frequencies, the Z' decreases with the increase in frequency for all the samples supporting a slow dynamic relaxation process in the sample, probably due to space charge that gets released at higher frequencies [26, 28–31]. Further, the lowest value of Z' at low frequency is obtained for pure KDC crystal of sample 1, which indicates the highest value of a.c. conductivity for that sample. As nickel is doped into the pure sample 1, the value of Z' increases, which shows decrease in the value of a.c. conductivity for the nickel-doped KDC crystals of samples 2 to 4. A particular frequency at which Z' becomes independent of frequency is observed to shift towards the lower frequency side after addition of nickel into pure sample 1 of KDC. This shifting in Z' plateau towards lower frequency side indicates the existence of frequency relaxation process in the samples [32] resulting into increase in grain relaxation time τ_g.

3.8 Frequency dependence of M'

Figure 9 shows the dependence of real (M') component of complex modules at room temperature of pure KDC and different mol% Ni-doped KDC. It is observed from the plot that in the lower frequency region, M' values are small, while on increasing frequency, a continuous dispersion takes place and M' reaches almost a constant value at higher frequencies. In the low-frequency region, the value of M' approaching zero, can be attributed to the removal of electrode polarization [33–35]. In the present case, negligible electrode polarization may be active in the lower frequency region. Further, in this region, the charge carriers are able to move within a long range path under the action of an induced electric field but due to lack of a restoring force governing the mobility of charge carriers under the effect of an induced electric field, the value of M' obtained is quite smaller [36, 37].

With increase in frequency, increase in the values of M' and reaching a maximum value at high frequency for all the samples can be attributed to the distribution of relaxation processes over a range of frequencies [38]. Further, at the higher frequency range, M' is found to exhibit highly dispersive nature which indicates increase in charge carrier hopping. The observed dispersion is mainly due to conductivity relaxation spreading over a range of frequencies and indicating the presence of a relaxation time, which is accompanied by a loss peak in the diagram of the imaginary part (M'') of electric modulus versus

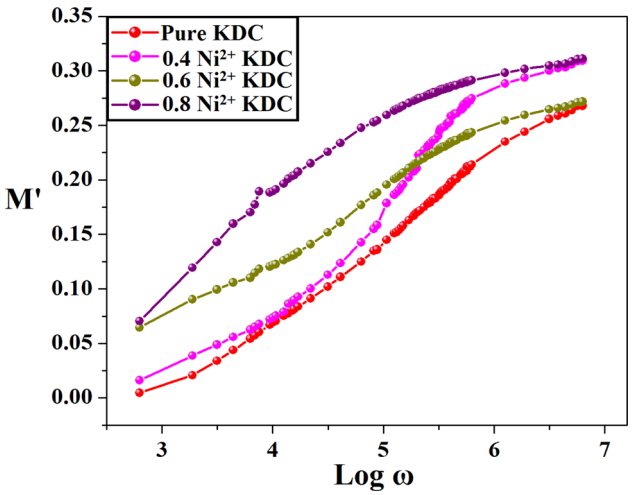

Fig. 9 Plot of M' versus logω of pure KDC and (0.4, 0.6, 0.8) Ni^{2+} doped KDC

frequency. In the present case, the value of M' increases after doping of different mol% of nickel in pure KDC. The enhancement in the values of M' after doping indicates decreased mobility of charge carriers.

3.9 Frequency dependence of Z''

Figure 10 shows the dependence of imaginary (Z'') component of complex impedance at room temperature of pure KDC and different mol% Ni doped KDC.

It is observed from the plot of pure KDC crystal shows a relaxation peak. The appearance of the peak at low frequency side indicates the grain boundary relaxation mechanism in the sample. The peak height is proportional to the grain boundary resistance (R_{gb}), as expressed in the equation $Z'' = R_{gb}\omega_m\tau / 1 + \omega_m{}^2\tau^2$, where ω_m is the relaxation angular frequency and τ is the relaxation time [39]. When different mol% nickel is doped into pure KDC, the peak is not observed but the trend of the plot shows that it might be shifted towards lower frequency region with increasing height indicating space-charge relaxation at lower frequency region [40]. However, the lower frequency region may be beyond the frequency measurement under study to observe this phenomenon. The increase in the peak height of different mol% nickel doped KDC crystals of samples 2 to 4 implies that the impedance of the samples 2 to 4 increases and shifting of the peak towards lower frequency region implies that the relaxation time τ increases. Further, Z'' are independent of frequency and merge together at higher frequencies due to the release of space charge in all the samples [36].

3.10 Frequency dependence of M''

Figure 11 shows the dependence of imaginary (M'') component of complex modulus at room temperature of pure KDC and different mol% Ni-doped KDC.

It is observed from the plot that M'' versus logω shows two peaks at different frequencies for pure KDC crystal. One at low-frequency ~ 1200 Hz is attributed to the grain boundaries mechanism and another one at high-frequency ~ 27,000 Hz is attributed to the grain mechanism. These peaks explain a well-defined two semicircles in the M^* plot. These peaks indicate the transition from short range to long-range mobility, with decreasing frequency. The low-frequency side of the peak represents the range of frequencies in which the ions are capable of moving long distances i.e., performing successful hopping from one site to the neighboring site, whereas for the high-frequency side, the ions are spatially confined to their potential wells and can execute only localized motion [41]. According to ideal Debye theory of dielectric relaxation, the impedance (Z^*) and the modulus (M^*) maxima peaks occurs at the same frequency and the full widths at half maximum (FWHM) of these peaks should be less than 1.14 decades [42, 43]. In the present case, the peaks of Z'' and M'' are not observed at the same frequency, i.e., Z'' peak observed at 300 Hz, while M'' peak observed at 1200 Hz. This indicates that the first

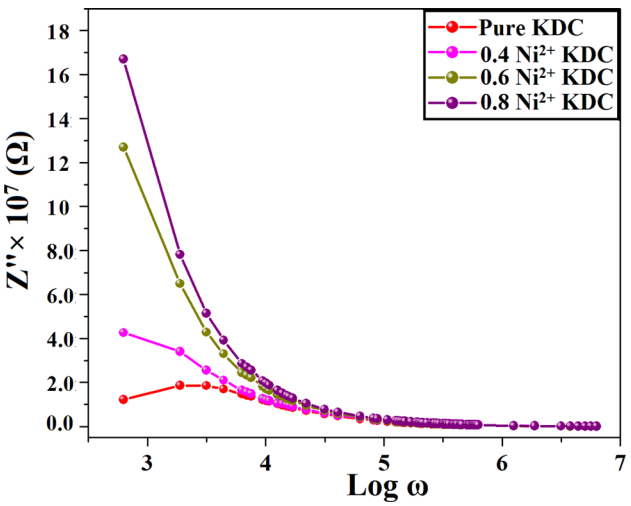

Fig. 10 Plot of Z'' versus logω of pure and (0.4, 0.6, 0.8) mol% Ni doped KDC

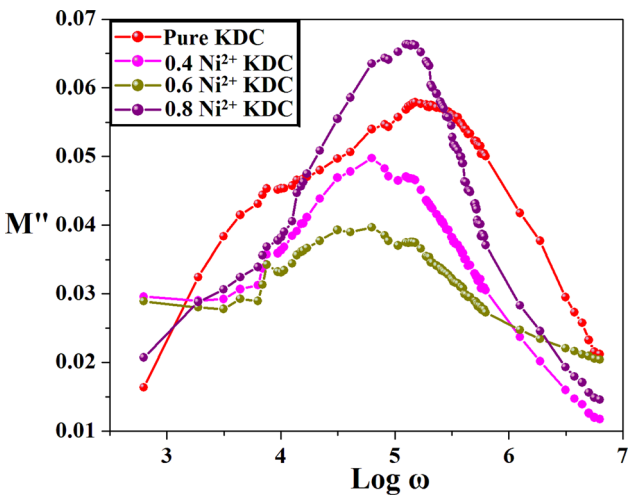

Fig. 11 Plot of M'' versus logω of pure KDC and different mol% Ni doped KDC

condition of ideal Debye type dielectric relaxation is not satisfied, resulting into the existence of non-Debye-type relaxation.

While in case of different mol% nickel is doped into pure KDC, the plot of M'' versus logω shows only one relaxation peak. The existence of one relaxation peak in such spectrum corresponds to grain effect only [36]. The shifting as well as change in magnitude of relaxation peak with temperature indicates the dependence of grain and/or grain-boundary capacitances as the case may be, on temperature [44]. In the present case, shifting of relaxation peak towards lower frequency side with change in magnitude of different mol% nickel doped KDC crystals shows the dependence of grain capacitance on the amount of dopant, i.e., different mol% of nickel. Further, the existence of broad and asymmetric peaks confirms the non-Debye behavior [35]. The region on the left of the peak is the region in which charge carriers are mobile over long distances, whereas the right of the peak is the region in which carriers are confined to potential wells being mobile over short distance [34, 35].

3.11 Complex modulus spectrum

Figure 12 shows the complex modulus spectrum at room temperature of pure KDC and different mol% Ni doped KDC. The modulus plane of pure KDC clearly shows two semicircles. The intercept of the first semicircle at low frequency side with the real axis indicates the total capacitance contributed by the grain boundary, while the intercept of the second semicircle at high frequency side indicates the total capacitance contributed by the grain [39]. From the intercepts of the plot on the real axis, the values of the grain boundary (C_{gb}) and grain (C_g) capacitances are found 57.25 pF and 34.96 pF, respectively.

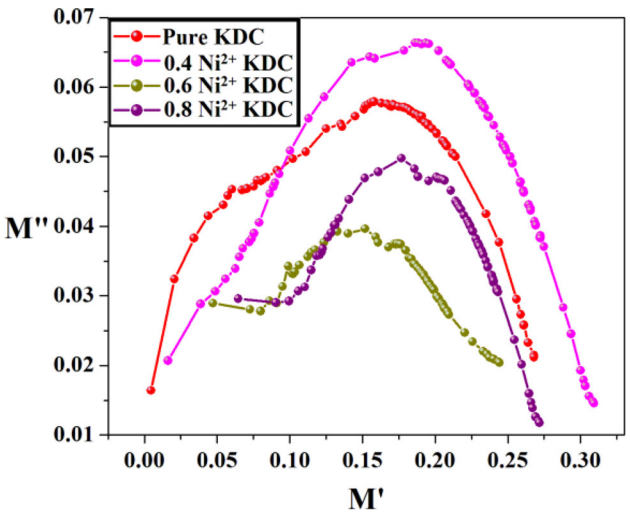

Fig. 12 Plot of M'' versus M' of pure and (0.4, 0.6, 0.8) mol% Ni doped KDC

The spectroscopic plot M'' versus logω and complex modulus plot M'' versus M' of pure KDC clearly shows two peaks as well as two semicircles, respectively. This clearly shows the presence of grain and grain boundary relaxation mechanism in the sample. The electrical modelling of these both relaxation mechanisms is simulated using the Z-view software, resulting into the two parallel R–C circuits connected in series. From the intercept of the first semicircle and second semicircle of complex modulus plot with real axis at low frequency side and high frequency side, respectively, the values of grain capacitance (C_g) and grain-boundary capacitance (C_{gb}) are calculated. Using the condition $2\pi fRC = 1$, the values of grain resistance (R_g) and grain-boundary resistance (R_{gb}) are calculated.

When different mol% nickel is doped into pure KDC, the complex modulus spectrum shows a single semicircle over the whole frequency considered, indicating the presence of gain contribution only. The prominent arc observed for all the different mol% nickel-doped KDC crystals can be attributed to the small capacitance of bulk, i.e. grain, indicating the presence of grain contribution only. The segments of the grain arc from the intersection on the M' axes are clearly visible for all the samples. The different capacitances of the grains and/or grain-boundaries contributions, whichever is present in the sample under investigation, give rise to arcs of different diameters in the plot [44]. In the present case, the different capacitances of the grain contributions present in the (0.4, 0.6 and 0.8) mol% nickel doped KDC crystals of are calculated from the intercepts of each plot with real axis and are obtained 42.48 pF, 30.18 pF and 36.41.

3.12 Modulus master curve

The modulus master curves of pure and different mol% Ni^{2+} doped KDC is shown in Fig. 13.

The modulus master curves reveals temperature dependence or independence of dynamic processes occurring within samples in terms of overlapping of master curves. Figure 13 indicates that all the master

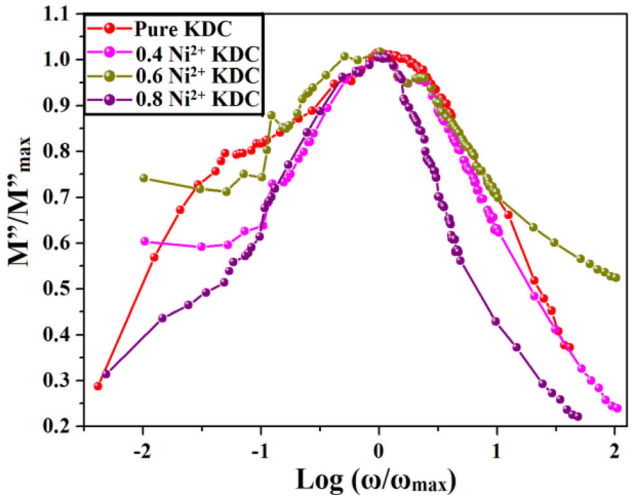

Fig. 13 Modulus master curves of pure and (0.4, 0.6, 0.8) mol% Ni^{2+} doped KDC

curves are found to be overlapped on each other but do not collapse into single curve and remains distinguishable which indicates temperature dependent relaxation within the samples. To decide nature of relaxation process occurring in pure and different mol% Ni^{2+}-doped KDC, the stretch exponent parameter (β) is computed by following equation:

$$\beta = \frac{1.196}{W} - 0.047, \tag{4}$$

where W is full width half maximum (FWHM) of M'' versus log ω curve obtained from Gaussian type curve fitting.

For grain and grain boundary relaxation, β—parameter is calculated, separated and summarized in Table 8.

Table 8 indicates deviation of β—parameter from unity due to decrease in concentration of Ni^{2+} doping indicates non-Debye type relaxation present within pure and different mol% Ni^{2+}-doped KDC crystals.

3.13 Complex impedance spectrum

To obtain a better understanding of polarization mechanisms that exist in the pure as well as different mol% nickel-doped KDC crystals t room temperature, complex impedance spectrum is drawn. This plot helps to separate out the resistances related to grain, grain boundaries and film/electrode interfaces because each of them has different relaxation times, resulting in separate semicircles in the complex impedance plane.

Figure 14 shows the complex impedance spectrum at room temperature of pure KDC and different mol% Ni-doped KDC.

The frequency increases in anticlockwise manner on the real (Z') axis, i.e., moving towards origin, frequency increases. The impedance property of the material is characterized by the appearance of single, double or even more semicircular arcs. One can observe the gradual process of change and development in such arcs either with change in temperature or with change in concentration of dopant. Such pattern gives the useful information about the types of electrical processes existing within the material. For such pattern, using a proper software, when an equivalent electrical circuit is prepared showing the similar behavior of the electrical processes existing within the material, one can establish a correlation with a microstructure of the material under investigation.

In the present case, the appearance of single arc or semicircle for pure KDC as well as for different mol% nickel-doped KDC can be attributed to the electrical properties in the materials arise mainly due to the contribution from bulk material (grain interior) and

Table 8 Stretch exponent parameter (β) for pure and (0.4, 0.6, 0.8) mol% Ni^{2+} doped KDC

Sample code	β_g	β_{gb}
Pure KDC	0.56	1.030
0.4 Ni^{2+}: KDC	0.62	–
0.6 Ni^{2+}: KDC	0.72	–
0.8 Ni^{2+}: KDC	0.81	–

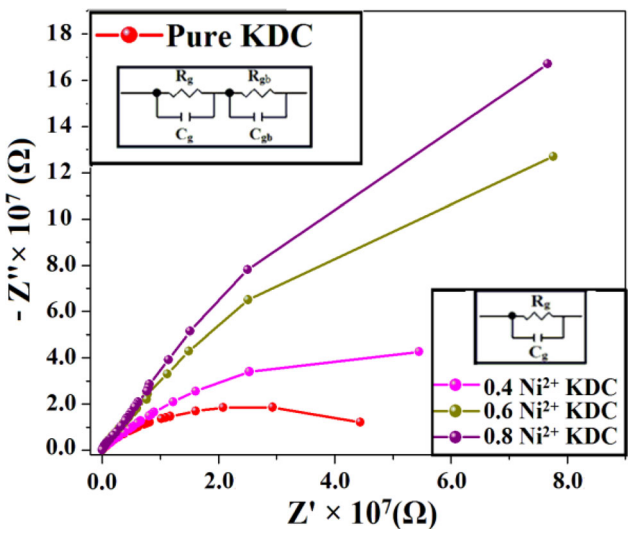

Fig. 14 Plot of Z'' versus Z' of pure and (0.4, 0.6, 0.8) mol% Ni^{2+} doped KDC

can be modeled as an equivalent electrical circuit consist of a parallel combination of bulk resistance and capacitance [37, 45]. The arc is almost semicircular for the pure KDC. As the different mol% nickel is doped into pure KDC, the semicircular arcs becoming larger and expanding from left to right of the Z' axis. This implies an enhancement in the diameter of the arcs for different mol% nickel doped KDC crystals which results in decrease in electrical conduction due to increase in resistance of these samples.

Note that within the frequency range under investigation, i.e., 100 Hz to 1 MHz, the complex modulus spectrum of pure KDC crystal, shown in Fig. 12 exhibits two semicircles and correspondingly two peaks in the plot of Fig. 11 of M'' versus logω, while the complex impedance plot of Fig. 14 shows a single semicircle and a single relaxation peak in the plot of Fig. 10 of Z'' versus logω in the low frequency region. Now, the appearance of single semicircle in the complex impedance spectrum can be attributed to the electrical properties in the material due to contribution of bulk effects. But in the spectroscopic plot of Z'' versus logω, the peak corresponding to grain relaxation mechanism is not observed in the high-frequency region.

This is because depending upon the magnitudes of R and C components, different situations may arise. For instance, if one of the capacitances is much larger than the other, its associated peak and semicircle will effectively disappear from the modulus plot [46]. Similarly, if one of the resistances is much lower than the other, its associated peak and semicircle may effectively disappear or become too small to observe from the impedance plot. The key point in determining whether RC elements are detected depends on which plot is used and the relative magnitudes of the capacitances. The modulus plots give emphasis to those elements with the smallest capacitances, whereas the impedance plots highlight those with largest resistances [46].

Here, to determine the values of the grain resistance (R_g) and grain boundary resistance (R_{gb}), the spectroscopic plot of M'' versus logω is used. The plot shows two characteristic peaks. The peak at low frequency side corresponds to the grain boundary relaxation mechanism and satisfying the condition $2\pi f_{max}R_{gb}C_{gb} = 1$, while the peak at high frequency side corresponds to the grain relaxation mechanism and satisfying the condition $2\pi f_{max}R_gC_g = 1$. Here, f_{max} corresponds to the relaxation frequency associated with each mechanism. By these relations, R_g and R_{gb} are evaluated and found to be 167.6 kΩ and 1.71 MΩ, respectively. The very low value of grain resistance (R_g) compared to grain boundary resistance (R_{gb}) may be responsible for the non-appearance of corresponding peak in the spectroscopic plot of Z'' versus logω of Fig. 10 and existing of too small semicircle near origin to observe from the impedance plot. The electrical modelling of grain and grain boundary effect is carried out by R–C parallel equivalent circuit shown by inset figure in Fig. 14.

When different mol% nickel is doped into pure KDC, the complex modulus spectrum shown in Fig. 12 exhibits single semicircle and correspondingly single peak in the plot of Fig. 11 of M'' versus logω in the high frequency region, while the complex impedance plot of Fig. 14 also shows a single semicircle and absence of relaxation peak in the plot of Fig. 8 of Z'' versus logω within the frequency range under investigation. The trend of the plot of Z'' versus logω, shown in Fig. 8 shows that it might be shifted towards lower frequency region with increasing height and hence, may be beyond the frequency measurement under study to observe this phenomenon. The presence of single semicircle for all the nickel-doped KDC in the complex modulus plot of Fig. 12 and appearance of relaxation peaks in the high-frequency region in the M'' versus logω plot shown in Fig. 11 confirms the presence of grain relaxation mechanism in the nickel doped KDC crystals. The value of grain resistance (R_g) for all the nickel doped KDC crystals is calculated by using the spectroscopic plot M'' versus logω shown (Fig. 11). In this plot, from the appearance of the peak, having different heights and positions at high frequency side, satisfying the condition $2\pi f_{max}R_gC_g = 1$, grain resistance R_g is evaluated for different mol% nickel doped KDC crystals and found to be 379 kΩ for 0.4 mol% nickel doped KDC, 347 kΩ for 0.6 mol% nickel doped KDC and 588 kΩ for 0.8 mol% nickel doped KDC.

From the above discussion, obtained equivalent circuit parameters are listed in the Table 9.

3.14 Dielectric studies

The variation in dielectric constant of pure KDC and different mol% nickel doped KDC crystals as a

Table 9 Equivalent circuit parameters for pure and different mol% Ni^{2+} doped KDC

Sample Nos	R_g (MΩ)	C_g (pF)	R_{gb} (kΩ)	C_{gb} (pF)	τ_g (ms)
Pure KDC	167.6	34.96	1.71	57.25	5.86
0.4 Ni^{2+}: KDC	379	42.48	–	–	16.10
0.6 Ni^{2+}: KDC	347	30.18	–	–	10.47
0.8 Ni^{2+}: KDC	588	36.41	–	–	21.41

function of frequency for all the samples is shown in the Fig. 15.

The nature of the plots shows high value of dielectric constant at lower frequency region for all the samples, which can be considered as a normal dielectric behavior [47] and then it is decreased with increase in frequency. The decrease in dielectric constant is significant especially at low frequencies which can be attributed to the presence of mobile nickel and potassium ion polarization and dipole polarization. As the frequency increases, the inadequacy of the dipoles to follow the applied a.c. electric field reduces the contribution of the charge carriers towards the dielectric constant, results into the decrease in the value of dielectric constant and tends to a static value.

Further, it can be noticed that the magnitude of dielectric constant is high for pure KDC. As nickel is doped in different mol% into pure KDC, the magnitude of dielectric constant decreases accordingly. The reason may be the formation of high resistive grain boundary as the nickel doping is increased (proved in the discussion of dependence of Z'' on frequency). Further, with nickel doping into pure KDC, the chemical pressure may be created in the nickel doped KDC, resulting into a possibility of change in the valances of different ions in the system, which results in increase in the resistance of grain (proved in complex impedance spectrum analysis), thereby reducing the probability of electrons reaching the grain boundary. This phenomenon may be the responsible factor for decrease in polarization and hence the dielectric constant.

Figure 16 shows the variation in dielectric loss as a function of frequency for all the samples.

The dielectric loss curves are exhibiting the higher values for all the samples at lower frequency and decreased gradually as frequency increases. The higher value of dielectric loss at lower frequency can be attributed to the presence of space charge polarization. Further, it is also evident that the magnitude of dielectric loss is high for pure KDC crystal decreases as different mol% nickel is doped into pure KDC. This behavior is similar to that of the dielectric constant, which can be explained in similar way as in the case of dielectric constant. Further, the conduction and relaxation components both may be

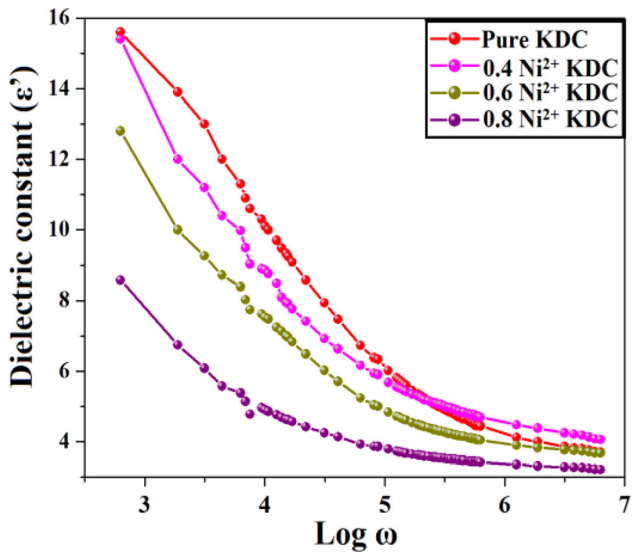

Fig. 15 Plot of dielectric constant versus logω of pure and (0.4, 0.6, 0.8) mol% Ni^{2+} doped KDC

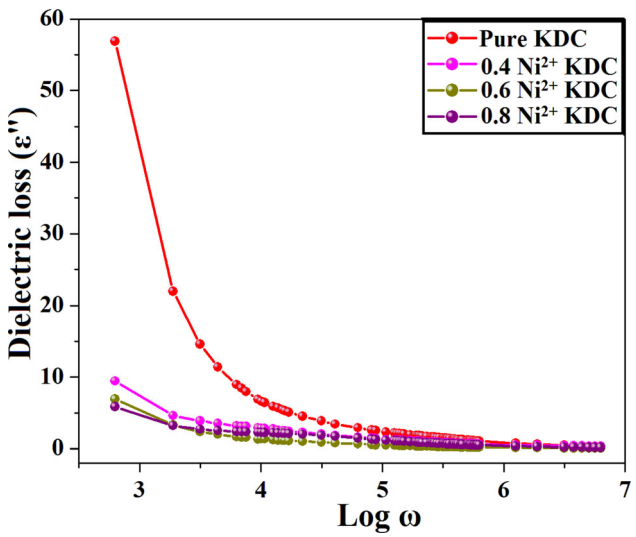

Fig. 16 Plot of dielectric loss versus logω of pure and different mol% Ni^{2+} doped KDC

postulated to contribute to the dielectric loss [44]. The contribution of d.c. conductivity to the dielectric loss can be explained on the basis of equation $\varepsilon'' = \sigma_{dc}/\omega\varepsilon_o$ [44], where ε_o is the vacuum dielectric constant, $\omega = 2\pi f$ is the angular frequency and σ_{dc} is the d.c. conductivity. The higher value of dielectric loss at low frequency can be attributed to the both d.c. conduction and relaxation processes. In the present case, the relaxation processes, i.e., the appearance of small relaxation peaks in the loss spectrum, are not observed in any of the four samples; hence the higher value of dielectric loss at low frequency can be attributed to the contribution arising from the d.c. conduction. At higher frequencies, d.c. conductivity no longer exists, hence relaxation losses are the only sources of dielectric loss. In the present case, no relaxation processes are observed in any of the four samples in the high frequency region also. Therefore, dielectric loss can be attributed to the relatively high resistivity and too low of upper level frequency used to show the resonance peaks.

3.15 A.C. conductivity analysis

The a.c. conductivity (σ_{ac}) values were calculated by using the expression $\sigma_{ac} = \omega\varepsilon_o\varepsilon''$, where ω is the angular frequency, ε_o is the permittivity of free space and ε'' is the dielectric loss [48].

Figure 17 shows the a.c. conductivity variation with respect to frequency for all the samples. From the Fig. 17, it is observed that the conductivity for pure and different mol% nickel-doped KDC crystals increases with increase in frequency. At higher frequency side, conductivity is observed more frequency dependent. This can be attributed to the transfer of charge carriers between different ions and liberation of charge carriers from the locations that restrict their movement. These liberated charge carriers participate in conduction process along with the electrons produced from the valence exchange between different metal ions. Further, conductivity is proportional to the product of mobility and carrier concentration. The present study is carried out at room temperature and hence carrier concentration remains constant within each sample. Therefore, conductivity depends on mobility and mobility increases with increase in frequency of the applied field. Thus, a.c. conductivity increases with frequency.

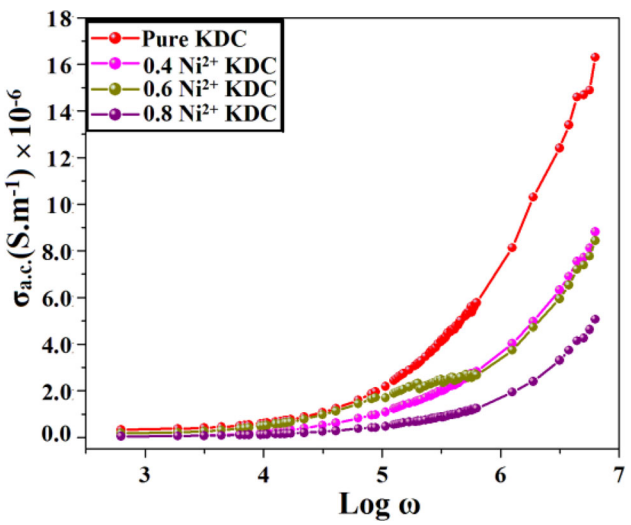

Fig. 17 Plot of a.c. conductivity versus logω of pure and different mol% Ni^{2+} doped KDC

It is also observed that the value of a.c. conductivity decreases for different mol% nickel-doped KDC crystals. This may be attributed to decrease in mobility and/or number of charge carriers due to a possibility of change in the valency of different ions in the system.

Figure 17 shows a low frequency flat or plateau region. A low-frequency plateau region in which conductivity remains frequency independent up to a certain frequency can be assigned to the d.c. conductivity of the samples, the value of which can be obtained by extrapolating the conductivity value to the lower frequency [49]. In this region, the transportation of the ions takes place on infinite paths [50], resulting into the much faster travel of the ions and jump from one site to another available site. The successful hoping of ions to a neighboring vacant site contributes to the d.c. conductivity [51].

The variation in a.c. conductivity of KDC due to different mol% Ni^{2+} doping can be attributed to formation of hydrogen bond defect by partial substitution of monovalent K^+ by bivalent Ni^{2+} ion to establish charge compensation. This hydrogen bond defect is developed in the form of unoccupied hydrogen bond (L-defect) and double occupied hydrogen bond (D-defect). The formation of D-defect is caused by trapping of freely moving H^+ produced due to charge compensation mechanism which ultimately reduces the conductivity. Thus, decrease in conductivity of different mol% Ni^{2+}-doped KDC crystals compared to pure KDC indicates that rate of formation of D-defect is large with compared to rate

of formation of L-defect. Furthermore, decrease in conductivity can be correlated by increase in impedance. Thus, Conductivity and Impedance curves are in correlation with each other. And hence, both are in correlation with hydrogen bond defect caused by Ni^{2+} doping.

3.16 Jonscher's plot

The frequency dependence of conductivity or so called universal dynamic response of ionic conductivity can be related by an expression given by Jonscher's power law [52], $\sigma_{total}(\omega, T) = \sigma_{dc}(T) + \sigma_{ac}(\omega) = \sigma_{dc}(T) + A(T)\omega^s$, where σ_{total} is the sum of d.c. and a.c. conductivity, σ_{dc} is the d.c. conductivity, $A(T)\omega^s$ is the a.c. conductivity due to the dispersion phenomena occurring in the material, $A(T)$ is a factor having the unit of conductivity, depends on temperature but not on ω and s is a power law exponent, which is a temperature and composition dependent quantity and generally varies between 0 and 1 [53]. The exponent s represents the degree of interaction between mobile ions with the lattice around them and A determines the strength of polarizability [54].

Figure 18 shows Jonscher's plot for pure and different mol% Ni^{2+} doped KDC, which shows highly dispersive behavior due to the existence of a.c. conductivity. The values of s and A can be calculated from the slope and intercept of the plot of Fig. 18 and listed in Table 10.

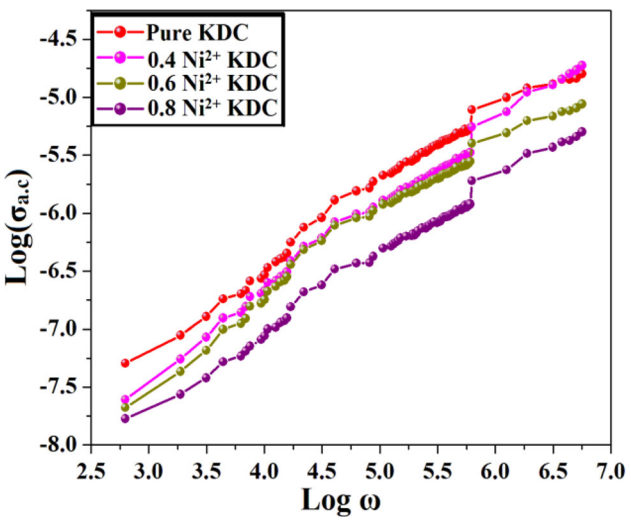

Fig. 18 Jonscher's plot of pure and (0.4, 0.6, 0.8) mol% Ni^{2+} doped KDC

From the Table 10, one can notice that highest value of strength of polarizability, i.e. the value of A, is obtained for the pure KDC. As different mol% nickel is doped into the pure KDC sample, the value of A decreases. In moving from 0.4 to 0.8 Ni^{2+} doped KDC, nickel content is increased gradually, which results into the gradual decrease in the value of A. As dielectric constant is directly related to polarizability of molecule, means greater the polarizability of molecule, higher is the dielectric constant of the material. On this basis, the value of strength of polarizability of pure KDC and different mol% nickel doped KDC are in accordance with the dielectric results. The value of the exponent s in Jonscher's equation is very useful in the prediction of conduction mechanism in the crystals. The value of exponent $s = 0$ indicates frequency independent or d.c. conduction [53], while $s = 1$ indicates that the interaction between neighboring dipoles is almost negligible [55, 56]. The value of $s \leq 1$ indicates that the hopping motion involved is a translational motion with a sudden hopping [57]. Usually, in case of ionic conductors, the value of exponent can lie between 0.5 and 1 indicating the ideal long range pathways and diffusion limited hopping [58]. In the present case, for all the samples, it is observed that the value of exponent s lies between 0.5 and 1 suggesting the above mentioned hopping. Further, the value of s is found to be low for the pure KDC crystal, which could be attributed to a high rate of successful jumps, results into high d.c. conductivity [59] as mentioned in Table 10. As the nickel is doped into the pure KDC, the value of s increases respectively. This could be attributed to the decreased rate of successful jumps of ions due to the presence of nickel at grain position, results into the decreased value of d.c. conductivity, respectively. Further, increased interaction between mobile ions and the lattice around them, leads to the reduction in the value of exponent s [60]. In the present case, the lowest value of exponent s for pure KDC, indicates the highest interaction between the charge carriers and lattice. The gradual increase in the value of exponent s due to the doping of nickel in the pure KDC leads to the decrease in the interaction between the charge carriers and lattice, which may be due to the presence of nickel at grain position.

Table 10 Conductivity mechanism related parameters for pure and (0.4, 0.6, 0.8) mol% Ni^{2+} doped KDC

Sample name	d.c. conductivity ($\sigma_{dc} \times 10^{-7}$) (S/m)	a.c. conductivity ($\sigma_{ac} \times 10^{-5}$) (S/m)	s	$A \times 10^{-9}$ (S m^{-1} rad^{-n})
Pure KDC	3.16	1.62	0.54	1.83
0.4 Ni^{2+}: KDC	1.66	0.882	0.66	1.19
0.6 Ni^{2+}: KDC	0.525	0.843	0.68	0.925
0.8 Ni^{2+}: KDC	0.385	0.506	0.70	0.621

3.17 Photo-luminescence (PL) study

In the present case, the excitation wavelength for PL absorption spectra is 254 nm and emission wavelength for PL emission spectra is 280 nm. Figures 19 and 20 shows the normalized PL absorption and emission spectra of pure and different mol% Ni^{2+} doped KDC.

The normalized emission spectra of each samples mainly consists of two major emission peaks. However, Ni^{2+} doping does not lead to change in emission peak numbers. Gaussian fitting is employed for clear identification of peaks which is shown in Figs. 21 and 22. Gaussian fit analysis of PL emission peaks is tabulated in Table 11.

By careful analysis of classification of emission wavelength from Table 11, the primary major emission peak is observed around 365–368 nm (UV emission) which corresponds to unoccupied hydrogen bond (L-defect) and the secondary major emission peak observed around (444–461) nm corresponds to double occupied hydrogen bond (D-defect).

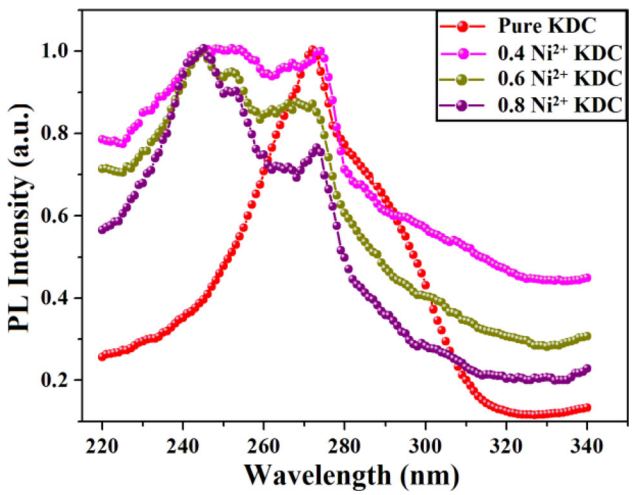

Fig. 19 Normalized PL absorption spectra of pure and (0.4, 0.6, 0.8) mol% Ni^{2+} doped KDC

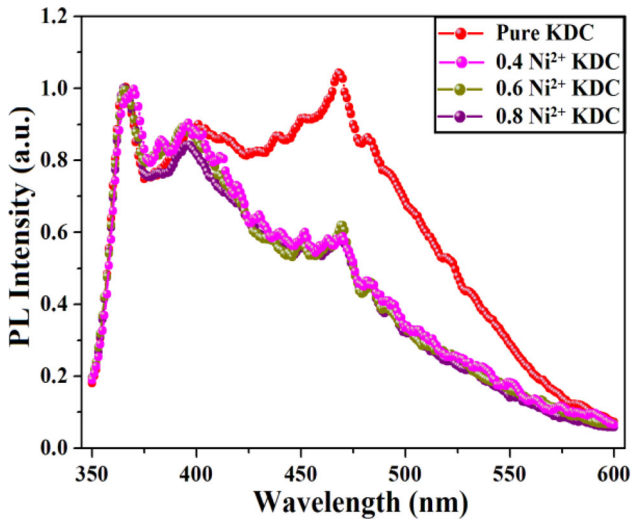

Fig. 20 Normalized PL emission spectra of pure and (0.4, 0.6, and 0.8) mol% Ni^{2+} doped KDC

Similar to KDC, existence of hydrogen valency due to deprotonation mode in sodium dihydrogen citrate is reported by Rammohan and Kaduk [61]. In the present case, Ni^{2+} doping produces L-defect in lattice of KDC and releases free H^+ ions (protons). These protons are trapped by oxygen containing functional groups due to higher electro negativity of oxygen which is 3.44. Such combination is known as double occupied hydrogen bond (D-defect). The lone pair of electrons contained by oxygen in oxygen containing functional groups tends to attract mobile protons produced by L-defect. As a result, D-defect produces hindrance in the motion of free protons which reduces the conductivity. The emission peaks and their corresponding defect state are mentioned in Table 12.

Figure 20 represents PL absorption spectra of pure and (0.4, 0.6 and 0.8) mol% Ni^{2+} doped KDC. The Gaussian fit analysis of PL absorption spectra is listed in Table 13.

For the same electronic transition, the wavelength difference between the position of band maxima of

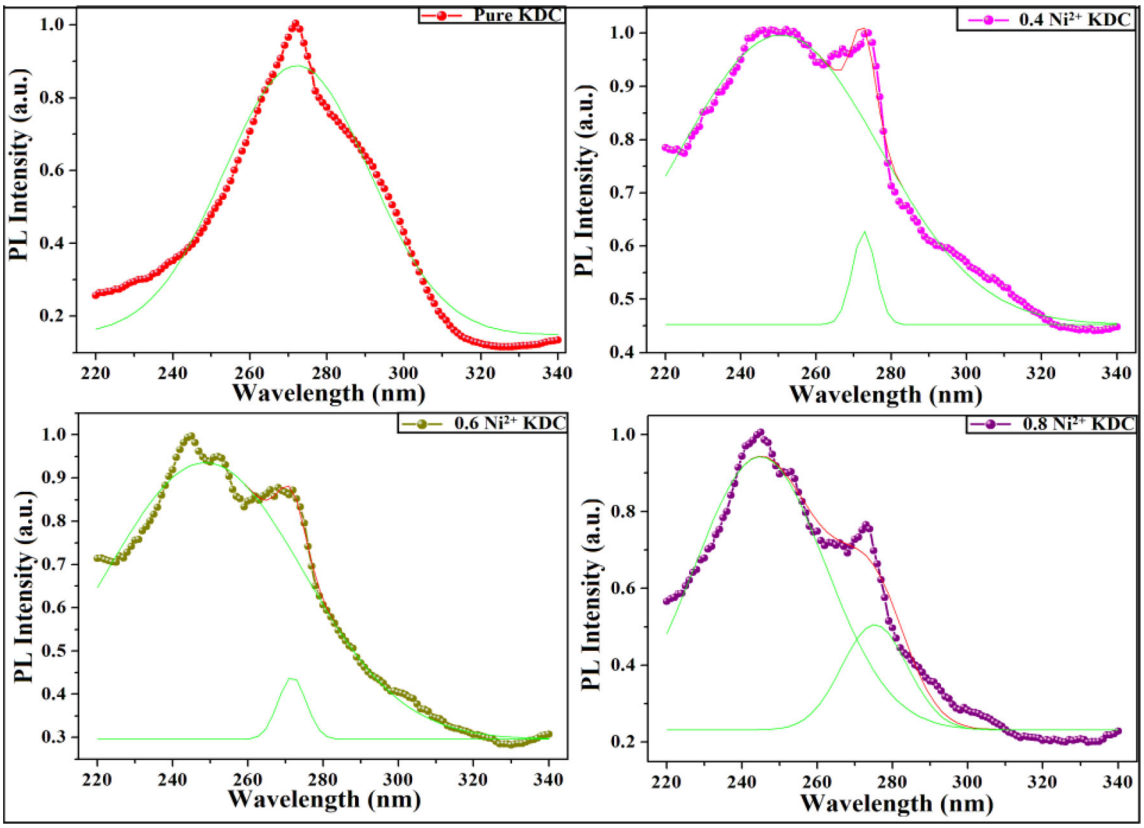

Fig. 21 Gaussian fitting of PL absorption spectra of pure and (0.4, 0.6 and 0.8) mol% Ni^{2+} doped KDC

absorption and emission spectra is defined as Stokes shift [62]. From the above wavelength difference, energy difference between absorption band maxima and emission band maxima is called Stokes shift. The existence of Stokes shift is the outcome of vibrational relaxation phenomenon [63]. The Stokes shift for pure and Ni^{2+} doped KDC crystals are listed in Table 14.

4 Conclusion

The pure and Ni^{2+} doped KDC crystals are grown by slow-solvent evaporation technique. The grown crystals exhibits triclinic symmetry and single phase nature with needle type morphology. The presence of Ni^{2+} at various doping concentration is identified by EDAX and the stoichiometric formulae are proposed. FT-IR spectroscopy leads to confirmation of various functional groups such as O–H, CH_2, O=C–H and their absorptions peaks gets slightly shifted in Ni^{2+} doped KDC with compared to pure KDC. TGA analysis reveals slight increase in thermal stability with increase in concentration of Ni^{2+} doping in KDC. SEM analysis indicates increase in grain size due to Ni^{2+} doping in host lattice of KDC.

The decrease in dielectric constant due to Ni^{2+} doping is attributed to increase in grain resistance. Pure and Ni^{2+} doped KDC crystals obeyed Jonscher's power law and parameter A and s are evaluated by linear fit of Jonscher's curves. The remarkable effect of Ni^{2+} doping in increasing hydrogen bond defect (D-defect) to acquire charge compensation is observed by PL studies and dielectric studies. Comparing Stokes shift of pure and different mol% Ni^{2+} doped KDC, Ni^{2+} is found to increase Stokes shift of KDC and decrease to the conductivity of KDC. The grain and grain boundary effects involved in crystals is successfully studied by impedance and modulus spectroscopy. It should be noted from Impedance–Modulus spectroscopic studies that pure KDC exhibits grain and grain boundary relaxation mechanism where as different mol% Ni^{2+} doped KDC exhibits grain relaxation mechanism only which is in correlation with increase in grain size confirmed by SEM analysis and evaluated by Debye–Scherrer's equation. R–C parallel equivalent circuit fitting is used to

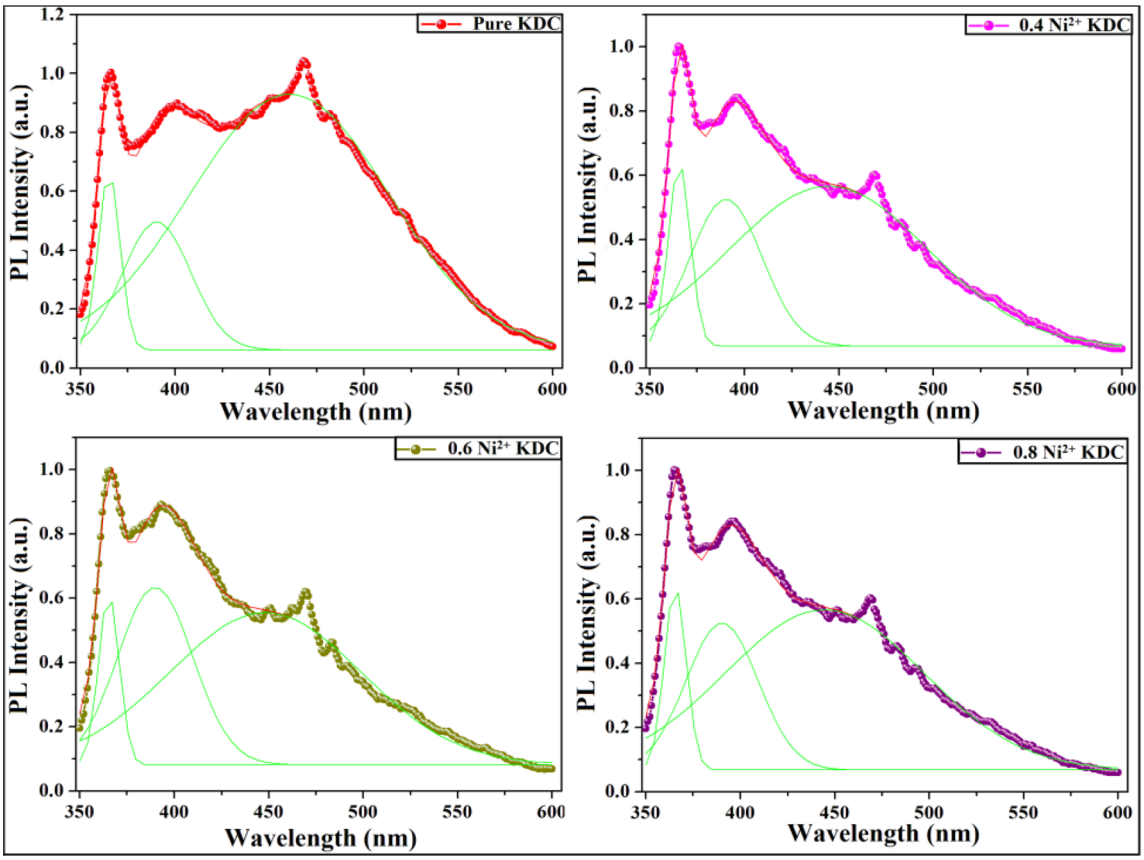

Fig. 22 Gaussian fitting of PL emission spectra of pure and (0.4, 0.6 and 0.8) mol% Ni^{2+} doped KDC

Table 11 Gaussian fit analysis of emission spectra of pure and Ni^{2+} doped KDC

Sr. Nos	Sample name	UV emission (nm)	Violet emission (nm)	Blue emission (nm)
1	Pure KDC	365.09, 390.34	–	460.59
2	0.4 Ni^{2+}: KDC	366.62, 391.61	447.26	–
3	0.6 Ni^{2+}: KDC	368.45, 394.28	446.27	–
4	0.8 Ni^{2+}: KDC	365.50, 390.26	444.62	–

Table 12 Emission peaks and their corresponding defect state in pure and (0.4, 0.6 and 0.8) mol% Ni^{2+} doped KDC

Sample name	Emission wavelength (nm)	
	L-defect	D-defect
Pure KDC	365.09, 390.34	460.61
0.4 Ni^{2+}: KDC	366.62, 391.61	447.26
0.6 Ni^{2+}: KDC	368.45, 394.28	446.27
0.8 Ni^{2+}: KDC	365.50, 390.26	444.62

Table 13 Gaussian fit analysis of absorption wavelengths for pure and (0.4, 0.6 and 0.8) mol% Ni^{2+} doped KDC

Sr. Nos	Sample code	Absorption wavelength (nm)	
1	Pure KDC	272.20	–
2	0.4 Ni^{2+}: KDC	234.79	257.31
3	0.6 Ni^{2+}: KDC	244.95	275.27
4	0.8 Ni^{2+}: KDC	250.31	273.14

evaluate grain and grain boundary resistance and capacitance. The relaxation peak is observed in Z'' versus logω curve which gets shifted in the lower frequency range indicating presence of space-charge relaxation in the samples.

Further, β-parameter lies between 0 and 1 indicating non-Debye type relaxation in the samples. The

Table 14 Variation in Stokes shift of pure and (0.4, 0.6 and 0.8) mol% Ni^{2+} doped KDC

Sr. Nos	Sample code	Absorption energy (eV)	Emission energy (eV)	Stokes shift (eV)
1	Pure KDC	4.56	2.69	1.87
2	0.4 Ni^{2+}: KDC	5.2806	3.3818	1.89
3	0.6 Ni^{2+}: KDC	5.0616	3.1446	1.91
4	0.8 Ni^{2+}: KDC	4.9532	2.7885	2.16

distinguishable nature of modulus master curves indicates temperature dependent relaxation phenomena in all samples.

Comparing the dielectric constants of pure and Ni^{2+} doped KDC, Ni^{2+} doping is found to decrease dielectric constant. Thus, dielectric constant of Ni^{2+} doped KDC may be used to detect toxic Ni^{2+} doping in low concentration in various food products by dielectric spectroscopy after proper standardization.

References

1. Potassium dihydrogen citrate: IN 332(i). www.foodnetindia.in
2. C. Sinclair, *Dictionary of Food* (A&C Black Publishers Ltd., London, 1998).
3. https://www.webmed.com/drugs/2/drug 8836//potassium.citrate-oral/details
4. S.C. Gad, Nickel and nickel compounds. Encycl. Toxicol. **3**, 506–510 (2014). https://doi.org/10.1016/B978-0-12-386454-3.00889-7
5. A.D. Sharma, Low nickel diet in dermatology. Indian J. Dermatol. **58**(3), 240 (2013). https://doi.org/10.4103/0019-5154.110846
6. W.E. Love, A.L. Patterson, X-ray crystal analysis of the substrates of aconitase, III, crystallization, cell constants and space groups of some alkali citrates. Acta Crystallogr. **13**, 426–428 (1993). https://doi.org/10.1107/S0365110X6000100X
7. D.E. Zacharias, J.P. Glusker, Structure of a citrate double salt: potassium di-hydrogen citrate–lithium potassium hydrogen citrate monohydrate. Acta Crystallogr. C **49**, 1727–1730 (1993). https://doi.org/10.1107/S0108270193002112
8. T.V. Van Auken, Solubility and heat of solution of potassium dihydrogen citrate. J. Chem. Eng. Data **36**, 255–257 (1991)
9. A. Marcilla, A. Gomez, M Berenguer Beltran, D Martinez, I Blasco (2017) TGA–FTIR study of the thermal and SBA-15-catalytic pyrolysis of potassium citrate under nitrogen and air atmospheres. J. Anal. Appl. Pyrolysis (2017). https://doi.org/10.1016/j.jaap.2017.04.007
10. Z. Aygun, AFM and SEM studies of VO^{2+} doped potassium dihydrogen citrate single crystal obtained by slow evaporation method. J. Chem. Crystallogr. **43**, 103–107 (2013). https://doi.org/10.1007/s10870-013-0391-4
11. Z. Aygun, Variable temperature EPR studies of Cu^{2+} and VO^{2+} doped potassium dihydrogen citrate ($C_6H_7KO_7$). Spectrochim. Acta **104**, 130–133 (2013). https://doi.org/10.1016/j.saa.2012.10.079
12. Z. Yarbaşi, A. Karabulut, B. Karabulut, EPR and optical studies of vanadium doped potassium dihydrogen citrate ($C_6H_7KO_7$) single crystal. Spectrochim. Acta **79**, 1304–1307 (2011). https://doi.org/10.1016/j.saa.2011.04.059
13. G.K. Williamson, W.H. Hall, X-ray line broadening from filed aluminium and Wolfram. Acta Metall. **1**, 22 (1953). https://doi.org/10.1016/0001-6160(53)90006-6
14. P. Scherrer, Bestimmung der Grosses und der inneren Struktur von Kollidteilchen mittels Rontgenstrahlen. Nachr. Ges. Wiss. Gott. **26**, 98 (1918)
15. J. Coats, in *Interpretation of Infrared Spectra, a Practical Approach*. ed. by R.A. Meyers (Wiley, Chichester, 2000), pp. 10815–10837
16. R.M. Silverstein, F.X. Webster, D.J. Kiemle, D.L. Bryce, *Spectrometric Identification of Organic Compounds*, 8th edn. (Wiley India Pvt. Ltd., New Delhi, 2019).
17. V. Mathivanana, M. Haris, T. Prasanyaa, Synthesis and characterization of gel-grown cobalt tartrate crystals. Pramana J. Phys. **82**, 537–548 (2014). https://doi.org/10.1007/s12043-013-0635-z
18. H.O. Jethva, P.M. Vyas, K.P. Tank, M.J. Joshi, FTIR and thermal studies of gel-grown, lead–cadmium-mixed levo tartrate crystals. J. Therm. Anal. Calorim. **117**(2014), 589–594 (2014). https://doi.org/10.1007/s10973-014-3770-y
19. S.J. Joshi, K.P. Tank, B.B. Parekh, M.J. Joshi, Characterization of gel grown iron–manganese–cobalt ternary levo-tartrate crystals. Cryst. Res. Technol. **45**(3), 303–310 (2010). https://doi.org/10.1002/crat.200900152
20. X. Sahaya Shajan, C. Mahadevan, FT-IR spectroscopic and thermal studies on pure and impurity added calcium tartrate tetrahydrate crystals. Cryst. Res. Technol. **40**, 598 (2005). https://doi.org/10.1002/crat.200410389
21. S.J. Joshi, K.P. Tank, P.M. Vyas, M.J. Joshi, Structural, FTIR, thermal and dielectric studies of gel grown manganese–copper mixed levo tartrate crystals. J. Cryst. Growth **401**, 210–214 (2014). https://doi.org/10.1016/j.jcrysgro.2014.01.060

22. G. Socrates, *Infrared Characteristics Group Frequencies* (Wiley, Chichester, 1980).
23. M.B. Bechir, K. Karoui, M. Tabellout, K. Guidara, A.B. Rhaiem, Dielectric relaxation, modulus behaviour and thermodynamic properties in $[N(CH_3)_3H]_2ZnCl_2$. Phase Transit. (2015). https://doi.org/10.1080/01411594.2014.987673
24. J. Ross Macdonald, *Impedance Spectroscopy, Theory and Applications*, 2nd edn. (Wiley, Hoboken, 2007).
25. A. Ala'eddin Saif, Z.A. Zahid Jamal, Z. Sauli, P. Poopalan, Mater. Sci. Medzg. **17**(2), 186 (2011)
26. J. Plocharski, W. Wieczoreck, Impedance spectroscopy and phase structure of PEO–NaI complexes. Solid State Ion. **979**, 28 (1988). https://doi.org/10.1016/0167-2738(88)90322-0
27. P. Ganguly, A.K. Jha, Structural, dielectric and electrical properties of $CaBa_4SmTi_3Nb_7O_{30}$ ferroelectric ceramic. Bull. Mater. Sci **34.**(4), 907 (2011)
28. J. Suchanicz, The low-frequency dielectric relaxation $Na_{0.5}Bi_{0.5}TiO_3$ ceramics. Mater. Sci. Eng. B **55**, 114 (1988). https://doi.org/10.1016/S0921-5107(98)00188-3
29. C.K. Suman, K. Prasad, R.N.P. Chaudhary, Impedance analysis of $Pb_2Sb_3LaTi_5O_{18}$ ceramic. Bull. Mater. Sci. **27**, 547 (2004)
30. M.R. Rangaraju, R.N.P. Chaudhary, J. Mater. Sci. **39**, 1765 (2004)
31. M. Rawat, K.L. Yadav, A. Kumar, P.K. Patel, N. Adhlakha, J. Rani, Structural, dielectric and conductivity properties of Ba^{2+} doped $(Bi_{0.5}Na_{0.5})TiO_3$ ceramic. Adv. Mater. Lett. **3**(4), 286 (2012). https://doi.org/10.5185/amlett.2012.2322
32. P.R. Das, B. Pati, B.C. Sutar, R.N.P. Choudhury, J. Mod. Phys. **3**, 870 (2012)
33. F. Yakuphanoglu, Electrical conductivity and electrical modulus properties of α, ω-dihexylsexithiophene organic semiconductor. Physica B **393**, 139–142 (2007). https://doi.org/10.1016/j.physb.2006.12.075
34. A. Dutta, T.P. Sinha, P. Jena, S. Adak, AC conductivity and dielectric relaxation in ionically conducting soda–lime–silicate glasses. J. Non-cryst. Solids **354**, 3952–3957 (2008). https://doi.org/10.1016/j.jnoncrysol.2008.05.028
35. S.B. Aziz, Z.H.Z. Abidin, A.K. Arof, Influence of silver ion reduction on electrical modulus parameters of solid polymer electrolyte based on chitosan-silver triflate electrolyte membrane. EXPRESS Polym. Lett. **4**(5), 300–310 (2010)
36. J.H. Joshi, G.M. Joshi, M.J. Joshi, H.O. Jethva, K.D. Parikh, Raman, photoluminescence, and a.c. electrical studies of pure and L-serine doped ammonium dihydrogen phosphate single crystals: an understanding of defect chemistry in hydrogen bonding. N. J. Chem. **42**, 17227 (2018). https://doi.org/10.1039/C8NJ03393E
37. P.R. Das, B. Pati, B.C. Sutar, R.N.P. Choudhury, Study of structural and electrical properties of a new type of complex tungsten bronze electroceramics; $Li_2Pb_2Y_2W_2Ti_4V_4O_{30}$. J. Mod. Phys. **3**(8), 870–880 (2012). https://doi.org/10.4236/jmp.2012.38114
38. L.N. Patro, K. Hariharan, AC conductivity and scaling studies of polycrystalline SnF_2. Mater. Chem. Phys. **116**, 81 (2009). https://doi.org/10.1016/j.matchemphys.2009.02.056
39. P.S. Sahoo, A. Panigrahi, S.K. Patri, R.N.P. Chaudhary, Impedance and modulus spectroscopy studies of $Ba_4SrSmTi_3V_7O_{30}$ ceramics. Mater. Sci. Pol. **28**(4), 763 (2010)
40. K.K. Bharathi, G. Marukandeyulu, C.V. Ramana, Impedance spectroscopic characterization of Sm and Ho doped Ni ferrites. J. Electrochem. Soc. **158**(3), G71–G78 (2011). https://doi.org/10.1149/1.3534800
41. J.S. Kim, Electric modulus spectroscopy of lithium tetraborate $(Li_2B_4O_7)$ single crystal. J. Phys. Soc. Jpn **70**, 3129 (2001). https://doi.org/10.1143/jpsj.70.3129
42. K. Prabakar, S.A.K. Narayandass, D. Mangalaraj, Cryst. Res. Technol. **37**, 1094 (2002)
43. J.H. Joshi, D.K. Kanchan, H.O. Jethva, M.J. Joshi, K.D. Parikh, Mater. Res. Bull. **93**, 63–73 (2017)
44. U. Ahmadu, S. Tomas, S.A. Jonah, A.O. Musa, N. Raibu, Adv. Mater. Lett. **4**(3), 185–195 (2013)
45. I.M. Hodge, M.D. Ingram, A.R. West, A new method for analysing the a.c. behaviour of polycrystalline solid electrolytes . J. Electroanal. Chem. Interfacial Electrochem. **58**(2), 429–432 (1975). https://doi.org/10.1016/S0022-0728(75)80102-1
46. D.C. Sinclair, Boi. Soc. Ceram. Vidrio **34**(2), 55 (1995)
47. J.C. Anderson, *Dielectrics* (Chapman and Hall, London, 1964), p. 16
48. R. Tripathi, A. Kumar, T.P. Sinha, Dielectric properties of CdS nanoparticles synthesized by soft chemical route. Pramana J. Phys. **72**, 969–978 (2009). https://doi.org/10.1007/s12043-009-0089-5
49. W.K. Lee, B.S. Lim, J.F. Liu, A.S. Nowick, AC conductivity in ionically conducting crystals and glasses. Solid State Ion. **831**, 53 (1992). https://doi.org/10.1016/0167-2738(92)90261-M
50. A. Dutta, C. Bharti, T.P. Sinha, Dielectric relaxation and ac conductivity study in $SrMg_{1/3}Nb_{2/3}O_3$. Indian J. Eng. Mater. Sci. **15**, 181 (2008)
51. K. Gohel, D.K. Kanchan, J. Adv. Dielectr. **8**, 185005(1–13) (2018)
52. A.K. Jonscher, The 'universal' dielectric response. Nature **256**, 673 (1977). https://doi.org/10.1038/267673a0
53. B.H. Bhat, R. Samad, B. Want, Appl. Phys. A **122**, 810(1–11) (2016)
54. C. Karthik, K.B.R. Varma, Dielectric and AC conductivity behavior of $BaBi_2Nb_2O_9$ ceramics. J. Phys. Chem. Solids **67**, 2437 (2006). https://doi.org/10.1016/j.jpcs.2006.06.012

55. K. Ngai, A. Jonscher, C. White, On the origin of the universal dielectric response in condensed matter. Nature **277**, 185–189 (1979). https://doi.org/10.1038/277185a0
56. P. Kour, P. Kumar, S.K. Sinha, M. Kar, Study of dielectric and impedance spectroscopy of La substituted nanocrystalline $Pb(Zr_{0.52}Ti_{0.48})O_3$ ceramics. J. Mater. Sci. Mater. Electron. **26**, 1304 (2015). https://doi.org/10.1007/s10854-014-2538-2
57. K. Funke, Jump relaxation in solid electrolytes. Prog. Solid State Chem. **22**, 111 (1993). https://doi.org/10.1016/0079-6786(93)90002-9
58. K.A. Mauritz, Dielectric relaxation studies of ion motions in electrolyte-containing perfluorosulfonate ionomers. 4. Long-range ion transport. Macromolecules **22**, 4483 (1989)
59. S.R. Elliott, A.P. Owens, The diffusion-controlled relaxation model for ionic transport in glasses. Philos. Mag. **60**(6), 777 (1989). https://doi.org/10.1080/13642818908209742
60. K. Sambasiva Rao, P. Murali Krishna, D. Madhava Prasad, T. Swana Latha, C. Satyanarayana, Indian J. Eng. Mater. Sci. **15**, 215 (2008)
61. A. Rammohan, J.A. Kaduk, A second polymorph of sodium di-hydrogen citrate, $NaH_2C_6H_5O_7$: structure solution from powder diffraction data and DFT comparison. Acta Crystallogr. E **72**(6), 854–857 (2016). https://doi.org/10.1107/S205698901600834
62. J.R. Gispert, *Co-Ordination Chemistry* (Wiley-VCH, Weinheim, 2008), p. 483
63. F. Hiroshi, J.E. Straub, Vibrational energy relaxation in proteins. Proc. Natl Acad. Sci. USA **102**, 6726–6731 (2005)